

The effects of powder feedstock and process parameters on the material characteristics of Ti6Al4V thin strut features fabricated by laser powder bed fusion additive manufacturing

Naresh Koju ^a, Jonah Hermes^b, Sumit Paul^a, Sayed Ehsan Saghaian^a, Li Yang^a

^a Department of Industrial Engineering, University of Louisville, Louisville KY 40292, USA

^b Department of Mechanical Engineering, University of Louisville, Louisville KY 40292, USA

Abstract

In this work, three different types of Ti6Al4V powder feedstock of different particle size ranges (fine, medium, and coarse) were utilized to fabricate thin strut lightweight features using laser powder bed fusion additive manufacturing (L-PBF-AM) using different process parameter settings. Thin strut features of varying dimensions from 0.1mm to 0.5mm were fabricated. The resulting sample sets allow for the analysis of the compound powder feedstock-process-geometry-material (PPG-M) characteristics for lightweight features fabricated by L-PBF-AM, which have not been previously explored. Various material characteristics were experimentally determined and analyzed, including success rate, geometry quality, porosity, pore size, grain size, and mechanical properties of the lightweight thin strut samples. The results clearly demonstrated the significance of the compound PPG-M relationships for lightweight structures, which calls for further studies to “re-establish” the knowledge base for L-PBF-AM materials at small dimension scales.

Keywords

Lightweight features, thin struts, powder feedstock, powder bed fusion, porosity, microstructure, strength

1. Introduction

Cellular structures are composed of interconnected networks of walls or struts or small unit cells (periodic or random) to achieve unique benefits such as a high strength-to-weight ratio, enhanced mechanical energy absorption, heat transfer control, and minimal material requirements [1, 2]. These unique benefits have attracted their use in different engineering applications such as biomedical implants, aerospace structures, automotive parts, sound insulation and damping, electrodes, heat exchangers, and other general lightweight designs [1-3]. Additive manufacturing (AM) is considered to be uniquely suitable for the realization of complex cellular structure designs due to its freeform geometry generation capabilities. However, one of the limiting factors for the adoption of AM cellular structure is the quality characteristics of the materials [4]. The cellular structure usually requires multiscale analysis involving unit cell macroscale and thin strut/wall microscopic levels. The responses at the microscopic structure level (i.e. cellular walls or struts) are more significantly influenced by the local material and process characteristics, as well as material anisotropy, which in turn affects the overall properties of the cellular structure [5]. Furthermore, simplistic periodic lightweight designs that are generally studied in the literature are actually not ideal for applications, and

often times optimization of lattice structures with varying wall thickness or strut diameters is needed for realistic designs [6]. Therefore, studies on the material characteristics of these thin features i.e., thin wall and thin strut are of particular interest.

Studies on the relationships between the material and mechanical characteristics of the thin features fabricated by laser powder bed fusion (L-PBF) and various design aspects such as feature geometry and the process parameters are available in the literature [7-15]. Current knowledge suggests rather complex correlations between L-PBF process parameters such as laser power and scan speed and the geometrical qualities of the Ti6Al4V micro-pillars (struts) and micro-plates (walls) [9]. The effects of feature orientation on the dimension, mechanical, morphological, and microstructural properties of L-PBF thin struts were also studied [6, 10-13]. Reduced geometrical quality with increased surface roughness and reduced cross-sections circularity was identified at lower-feature orientation angle struts [10, 13]. Murchio et al. [13] reported that the feature orientation directly affects the surface texture and geometry-induced surface imperfections attributed to different thermal behavior history and staircase effect, and plays a vital role in the thin feature's fatigue life. Vrána et al. [14] developed process window for L-PBF process strut-based cellular structure fabrication using different levels of overlaps of contour scans only to achieve controlled porosity and roughness level based on combination of input energy density.

Weißmann et al. [11] performed a comparative study between L-PBF and electron beam powder bed fusion (EB-PBF) of Ti6Al4V struts. The slenderness ratio, which was defined as the ratio between the effective length and the gyration radius of the fabricated strut, was shown to be correlated to both the compressive strength, equivalent diameter and height of the struts. L-PBF struts showed higher dimensional accuracy, significantly lower roughness R_a and R_z than the EB-PBF struts. In addition, the struts fabricated by the two types of PBF processes exhibit different hardness due to different microstructures induced by their respective thermal histories. Leicht et al. [12] reported that in the PBF process both the part geometry and feature orientation exhibit significant effects on the microstructure and texture of the thin features. For thin wall features, heterogeneous nucleation takes place from individual powder particles at the boundaries, with subsequent grain growth towards the interior center following the maximum temperature gradient. Since the grain growth near the boundary is inhibited by higher cooling rate, with the increase of thin wall thickness, the amount of large elongated grains with a more pronounced texture oriented parallel to the building direction also increases. A study performed by Wang et al. [15] on stainless steel 316L vertical struts reported no clear trend of columnar grain width along the build direction with variation of the strut diameter. However, preferred grain orientation begins to appear with the decrease of strut diameter.

Feedstock powder characteristics such as particle size and its interplay with layer thickness plays an important role in the PBF process characteristic and is related to various part quality aspects such as density, surface quality, accuracy, internal defects, static mechanical properties and fatigue properties [16-26]. During the process of PBF, powder flowability/rheology has significant effect on the formation of homogenous powder layer. Generally, the flowability increases with decrease of particle size distribution (PSD) range, improves with coarser particles and decreases with increase in moisture content until saturation point [16, 18, 19, 26]. Balbaa et al. [26] reported the presence of refined cellular microstructure while using the coarse AlSi10Mg powder feedstock, which resulted in higher microhardness with the fabricated parts

compared to those fabricated using fine powder feedstock. On the other hand, depending on the powder spreading mechanism, a bi-modal PSD distribution with refined powder mixed in coarser powder could benefit the powder bed density and the subsequent part quality, due to the filling of the inter-particle voids among larger particles by the small-size particles [17, 22]. Groarke et al. [27] reported improvement of powder flow with the presence of fine particles in the feedstock. In addition to the powder feedstock PSD, the shape of the particle/ morphology also has significant effects on powder rheological properties [19, 20]. For non-refined powder feedstock, spherical particle shape facilitates the powder packing efficiency and powder flowability compared to non-spherical or irregular-shaped particles [16, 19].

In comparison, literature about the effect of powder feedstock on the process characteristics, geometry accuracy and material characteristics of the thin features ($< 1\text{mm}$) is much more limited. The studies on single track powder bed fusion can be useful in understanding of thin feature process characteristics due to their dimensional similarity. A multi-layer single track L-PBF-AM process simulation study conducted by Cao and Guan [28] showed that the surface roughness increases with increase in proportion of large-size particles. In addition, the presence of higher proportion of small-size particles at smaller layer thickness ($30\mu\text{m}$) and lower proportion of larger-size particles at larger layer thickness ($45\mu\text{m}$) led to lower porosity. In general, there still exist significant knowledge gaps in the compound powder feedstock-process-geometry-material (PPG-M) characteristics for lightweight features fabricated using L-PBF. Therefore, in this work, three different powder feedstocks (fine, medium, and coarse) were utilized, and thin struts of varying dimensions were fabricated via various process settings using these powder feedstocks for the characterization of the PPG-M characteristics of these lightweight features. Various process and material characteristics such as fabrication success rate, geometrical accuracy, porosity, pore size, microstructural grain width and mechanical properties were investigated. Due to the large dimension of the comprehensive PPG-M characteristics, some of the input variables that are expected to be also significant such as feature orientation angle, layer thickness and scan strategy were not included in the experimental design of this study. It was anticipated that the results from this work could provide new qualitative insights into the PPG-M relationships, while more quantitative and comprehensive understanding of the dimension-dependent process characteristics would likely require additional investigation via a combination of both experimentation and process modeling.

2. Experimental methods

2.1. Powder Feedstock characterization

Three powder feedstocks with varying particle size ranges were purchased from Praxair Surface Technologies, Inc., namely Ti-105-1 (Medium powder, $D_{50}=12.48\mu\text{m}$, $D_{10}-D_{90}$: $6.29-19.65\mu\text{m}$), Ti-105-13 (Fine Powder, $D_{50}=37.31\mu\text{m}$, $D_{10}-D_{90}$: $24.41-55.62\mu\text{m}$), and Ti-105-27 (Coarse Powder, $D_{50}=72.15\mu\text{m}$, $D_{10}-D_{90}$: $57.35-94.69\mu\text{m}$), all gas atomized. The particle sizes of each powder feedstock were characterized using Microtrac S3500 particle analyzer. The particle size distribution curves for the three types of powder feedstock are shown in Fig.1. To further characterize the powders, both tap density and powder bed density were measured. For powder bed density evaluation, powder from each type of feedstock was spread by the powder spreading actions layer by layer in the system (EOS M270) with no laser melting actions. A total of 10mm-thick powder was spread, and all the powder from the entire build bed was subsequently

retrieved carefully. The powder bed density was then calculated by dividing the weight of the powder by the overall build volume. A very small amount of powder was expected to be lost during the manual powder retrieval process, however due to the sufficiently large overall volume of evaluation, such error was considered negligible.

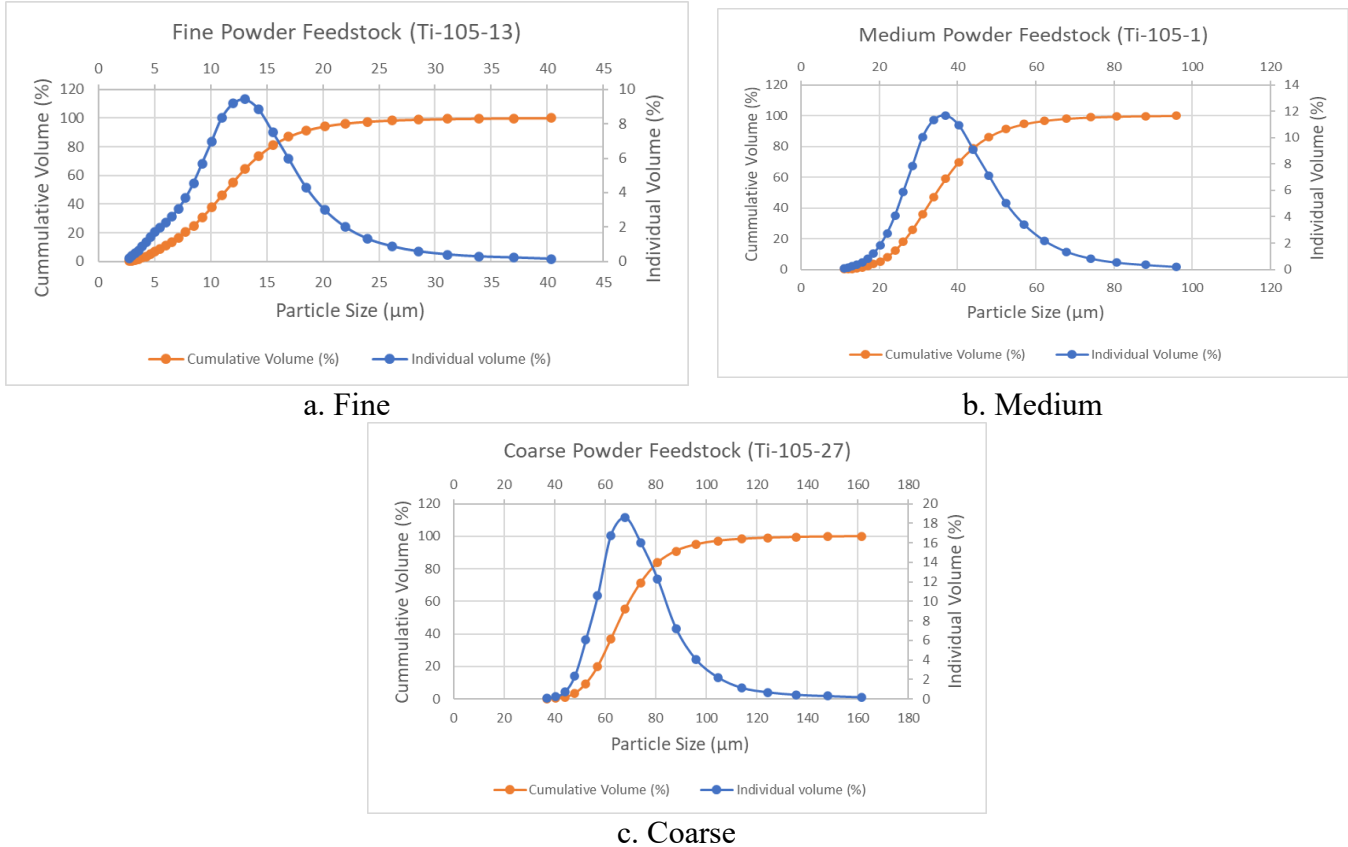


Figure 1: Powder feedstocks particle size distribution

2.2. Experimental design and sample fabrication

For the thin strut geometry, diameter of 0.1mm, 0.3mm and 0.5mm were designed. The overall length of the thin struts of 0.1mm, 0.3mm and 0.5mm were set as 5mm, 8mm and 10mm, respectively. The main consideration of the length designs was to accommodate handling and experimental setup (e.g., sample cutting and mounting), as the length-to-diameter ratios of all the designs were considered sufficiently large (>20) for the struts to be considered slender beams. All the thin struts were orientated at 75° (in relation to x-y plane), which was arbitrarily selected. Fig. 2 shows the design and as-built thin strut samples. For the thin strut samples, encircling wall features were designed in order to provide protection to the rather fragile sample during the post-fabrication cutoff. The samples were fabricated by the EOS M270 system. Multiple levels of laser power (90W, 100W, 110W) and scan speed (360mm/s, 400mm/s, 440mm/s) were investigated, as shown in Table 1. The choice of the baseline parameter level (80W +400 mm/s) was based on the default support scan strategy for Ti6Al4V with the EOS M270 system. Other process parameters were kept constant but are also noted here due to their relevance in the fabrication process. The layer thickness and hatch spacing distance of 30μm and 100μm were employed, which are both default for the processing of Ti6Al4V in the system. Both contour

scan and hatch scan were enabled for all the samples. The hatch spacing scan of x-direction with 45-degree rotation on exposure was set. The process experimental design is shown in Table 1. For each setting, 5 replicates of the thin strut sample were fabricated.

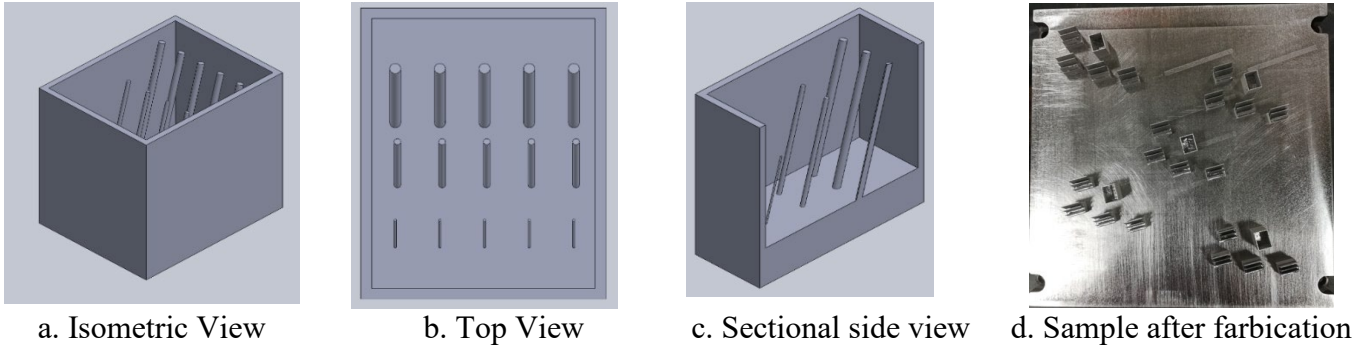


Figure 2: (a-c) Thin Strut CAD designs and (d) actual sample after fabrication

Table 1: Experimental design for process parameter settings

Powder Feedstock		Fine, Medium, and Coarse	
Thin Strut Diameter		0.1 mm, 0.3 mm, and 0.5 mm	
Powder Layer Thickness		30 μm	
Hatch Scan Spacing		100 μm	
Part Orientation		75°	
Notation	Laser Power (W)	Scan Speed (mm/s)	Volume Energy Density ($\text{J}\cdot\text{mm}^{-3}$)
P1 (Baseline)	100	400	83.33
P2	100	360	92.59
P3	100	440	75.76
P4	90	400	75.00
P5	110	400	91.67

2.3. Sample preparation and characterization

After fabrication, the samples were carefully cut from their support structures using an Allied TechCut 5 slow cutter. To prevent damage or loss, the chambers of the thin strut samples were filled with candle wax prior to cutting, as shown in Fig. 3. The wax was removed afterwards by simply heating the samples.



Figure 3: Thin Strut Sample retrieval using wax

The as-built samples were subjected to further characterization without stress-relieving. Thickness measurement was carried out using digital optical microscope (Olympus MX51) by taking three locations along the length of the samples and measuring the thickness from the two external boundary points within focus. One of the replicates of each sample design was grinded along the x/y-z plane and mounted with epoxy resin into metallurgical samples for porosity and microstructural analysis. For the metallurgical sample preparation, the samples were carefully grinded to roughly half-planes by a Pace Technologies NANO 2000T sample grinding/polishing machine using 180/240 and by a semi-automated Allied MetPrep 3 Grinder/Polisher using 400-grit sandpapers. After achieving the desired sample planes, the samples were further polished with a polishing grit number sequence of 600, 800 and 1200 grit sandpapers, followed by 6 μ m and 1 μ m diamond suspension polishing with polishing lubricant in the same Grinder/Polisher at 100-150 rpm. Polished samples were first subjected to porosity characterization, including areal porosity and areal pore size measurements. For each sample, the porosity and pore sizes were measured at three different build heights (near support, middle, and large height). Image analysis-based porosity characterization was carried out using ImageJ software. While the gas pores and keyhole pores are typically spherical in shape, lack-of-fusion flaws can be large and irregular in shape [29]. A study performed by Gong et al. on defect morphology in Ti-6Al-4V parts manufactured using L-PBF process showed the defect circularity ranging from approximately 0.10 – 1.0 for process settings at over-melting zone [30]. With the aim to capture defects as small as single-micron size and the ones with low circularity, the pore size of greater than 2 μ m² and circularity of 0.10-1.0 were used as identification thresholds. The lower limit of defect cross-sectional area of 2 μ m² corresponds pores with ~ 1.4 μ m diameter with a circular cross-section which was identified to be reasonable cut-off limit based on the experimental PSD results. Afterwards, the samples were then etched with Kroll's reagent for microstructural analysis using cotton swab rubbing. The exact etching times varied from approximately 25 to 35 seconds depending on the reagent available on the sample during swab rubbing and sample size. The completion of etching was determined by frequently inspecting the microstructural image quality under the optical microscope. The etched samples were subjected to grain width measurement using linear interception following ASTM E112-13 (Heyn Lineal Intercept Procedure) [31] using the digital optical microscope. It is also noted that for the thin strut samples the physical exterior boundaries themselves also count as grain boundaries, which differs slightly from typical procedures. Since the large-size grains mostly exhibit columnar morphology with orientations generally along the z-direction (build direction), the intercept lines were selected to be approximately perpendicular to the z-direction.

The remaining 0.3 mm and 0.5 mm samples were subjected to a three-point bending test to evaluate their mechanical properties, due to the difficulty of sample gripping for typical tensile testing. The 3-point bending test setup is shown in the Fig. 4. The mechanical testing was performed on the Mark-10 ESM306 tensile testing machine with 500N load cell and a custom 3-point bending fixture, under a constant loading rate of 0.50 mm/min and span length of 4mm. The sample was slightly preloaded to ensure proper contact between the upper anvil and test sample. The equipment lowest loading rate was used such that the kinematic effects such as slippage can be minimized. The samples were tested till the failure which was identified by 70% drop in the applied load.

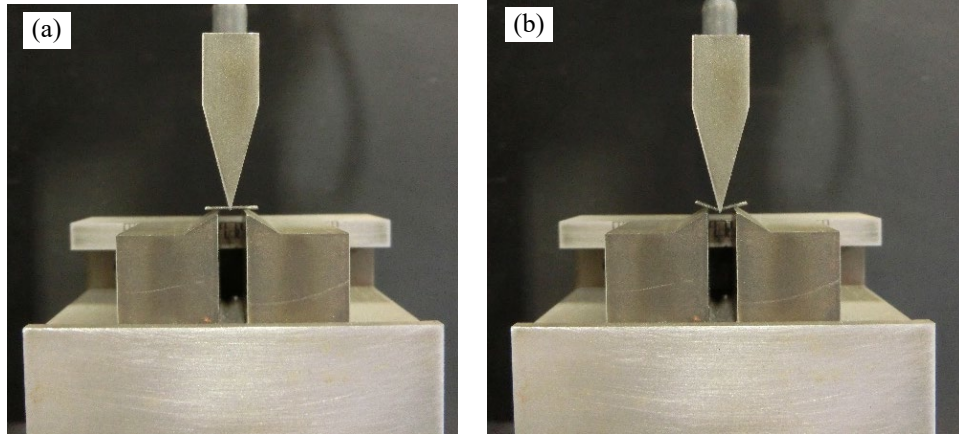


Figure 4: Three point bending test setup (a) before testing (b) after testing

3. Results and discussion

3.1. Feedstock powder characteristics

The densities of the three types of feedstocks are listed in Table 2. Considering the Ti6Al4V material density to be 4.43 g/cm^3 , tap density and powder bed density were normalized. The fine powder exhibits the highest tap density but the lowest powder bed density. This is likely due to the enhanced inter-particle interactions at reduced particle sizes, which causes low flowability but could be overcome with additional powder fluidization mechanisms such as vibration. The relatively broad relative PSD range of the fine powder might also contribute to the high tap density of the powder feedstock. Although the absolute particle size range for the fine powder is narrow ($\sim 14\mu\text{m}$ between D_{10} and D_{90}), the percentage size range is rather significant (D_{90} approximately 300% of D_{10}). Consequently, the void-filling effect from polydisperse powder packing is more pronounced [32]. On the other hand, the medium feedstock exhibits the lowest tap density and highest powder bed density, which might be partially explained by its good flowability and spreadability, as well as the relatively narrow relative PSD range.

Table 2: Different Powder feedstock densities

Powder Feedstock	Tap density (g/cm^3)	Normalized Tap density	Powder Bed density (g/cm^3)	Normalized Powder Bed density
Fine	3.29	0.743	2.33	0.526
Medium	2.86	0.646	2.79	0.630
Coarse	3.23	0.729	2.66	0.600

3.2. Fabrication success rate

The success rates of the thin strut fabrication under each design condition were estimated by the percentage of successfully fabricated samples. Due to limited sample replication number (5), the success rates were estimated in rather crude scales. However, it was expected that such information could still provide some insights into the effects of different design input variables. As shown in Fig. 5a, the success rate for 0.1mm thin struts are higher with fine powder feedstock

whereas for 0.3 mm and 0.5 mm thin struts coarse powder feedstock showed highest success rate. The success rate of the 0.1mm strut is higher with the fine powder feedstock, which might be resulted from the reduced variability of melt pool-powder interaction due to the larger average numbers of powder particles involved. On the other hand, for 0.3mm and 0.5mm struts, the lower powder bed density of the fine powder feedstock likely become a significant factor for defect generation and consequently lower success rates. It could be reasonably speculated that for the thin feature fabrication, refined powder could favor the stability of melt pool evolution, which is more critical for features with shorter melt pool continuity (e.g., thin struts of small dimensions). Although the powder feedstocks investigated in this study all exhibit single-modal PSD, it could be expected that a feedstock with bi-modal PSD might be optimal for the fabrication of thin struts, as the fine powder serves to stabilize the melt pool evolution while the overall flowability/spreadability of the feedstock is ensured.

Fig.5b–d provides further insights on the effect of energy density, scan speed and laser power on the success rates of thin struts. The thin struts exhibit higher success rate at lower energy density level. A study conducted by Gong et al. [33] on bulk features identified the energy density window of approximately 35.34-60.78 J/mm³ for fully dense parts. Promopattum et al. [34] recommended a similar energy density window of 36.9-87 J/mm³ for fully dense part. The energy density levels investigated in this study were set near the high end of the suggested range. In addition, due to the kinetic inertia effect with the mechanical laser deflection system (i.e., the galvanometer system), the actual dwell times of laser within the processed regions is likely higher than the nominal values, which corresponds to higher-than-nominal input energy density. This might partially explain the observed trend in this study. Except for 0.1mm samples, decrease in laser power and increase in scan speed improved the fabrication success rate (Fig.5c–d) as they result in lower energy densities.

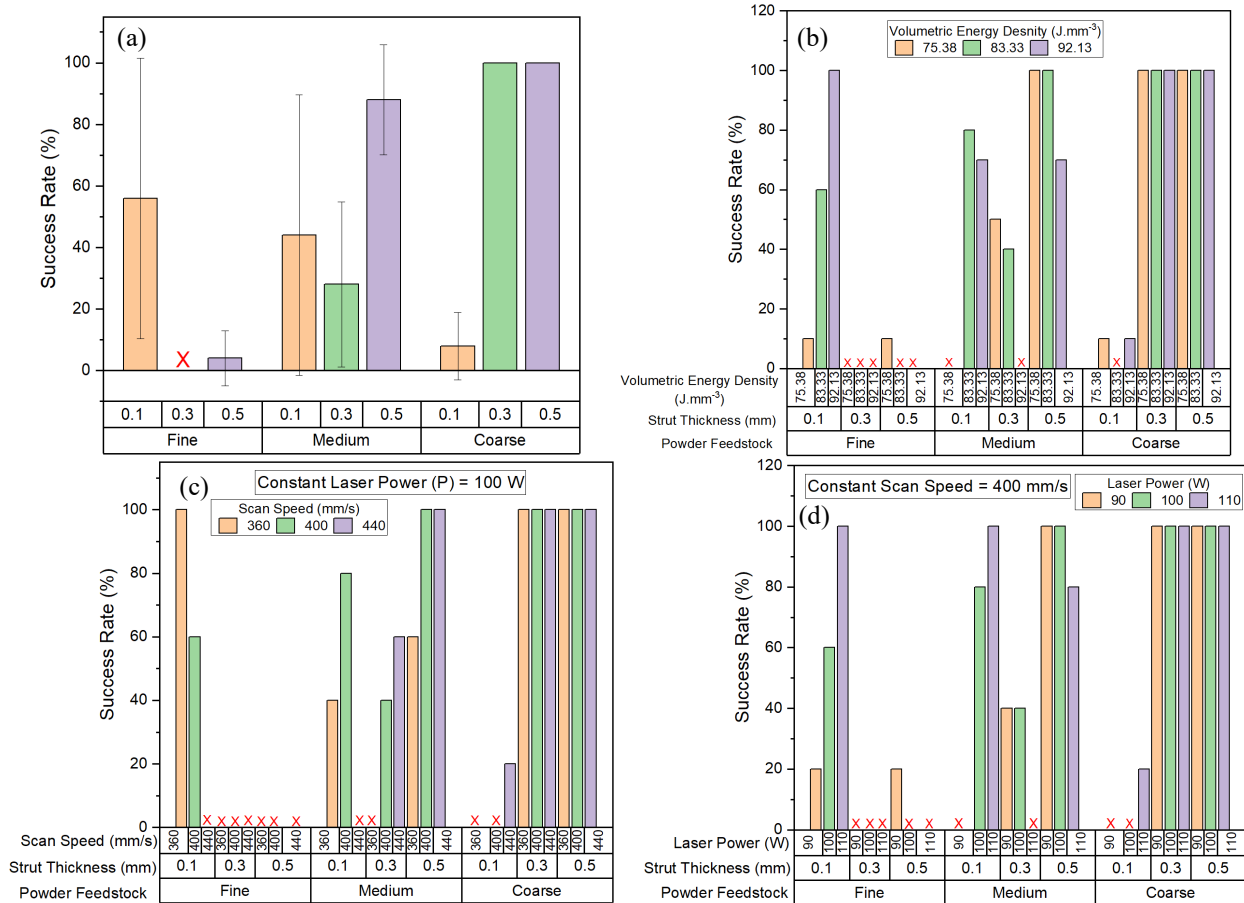


Figure 5: Success rate of thin struts (a) all samples (b) at different conventional energy densities (c) at constant laser power of 100W (d) at constant scan speed of 400 mm/s. The red 'X' represents complete missing sample.

3.3. Effects on dimensional accuracy

Fig. 6 shows the geometrical accuracy of thin struts feature in terms of absolute error and relative error (%). Absolute error is the different between the measured strut diameter and designed strut diameter, whereas relative error is the percentage of absolute error with respect to the designed strut diameter. A trend of increase in dimensional error (i.e., decrease in dimensional accuracy) with increase in feedstock size can be observed. Although the energy density has low significance, indication of higher dimensional accuracy was identified at lower energy density. Higher dimensional accuracy was observed with the increase in dimension. The absolute errors for fine and coarse feedstock samples appear to converge to approximately 90 μ m and 150 μ m respectively. With the utilization of optimum process settings, it is believed that the fine powder samples can generate higher success rate and dimensional accuracy with thin features. The fuse of partially sintered un-melted powder to the melted powder on the part surface due to insufficient heat input on the edge borders of samples is expected to be the main cause for the dimensional error, and exerting higher impact on lower dimension samples as such effect is expected to be similar to samples regardless of their dimensions [35-38]. The present study utilized high input energy density that leads to over-melting, thus it will be potentially beneficial to investigate lower energy density levels in future studies. As current study energy

densities are in over-melting zone, the decrease in energy density is generally favorable for reduced dimensional error. In addition, coarse powder feedstock with largest powder particle size appears have lowest geometrical accuracy, which implies significant role of powder feedstock type geometrical accuracy of thin features as compared to investigated range of energy density in. Table 3 lists the optical microscope images of thin struts fabricated with different powder feedstocks. These images clearly show the impact of sintered un-melted powders on the dimensional accuracy specially for the coarse powder feedstock.

Table 3: Optical Microscope images thin features built using different powder feedstocks

Powder → Structure ↓	Fine powder	Medium Powder	Coarse Powder
Strut (\emptyset 0.1mm – Fine; \emptyset 0.3mm – Medium and Coarse)	L1=165.63um	L1=378.59um	L1=422.54um
	L2=183.66um	L2=357.18um	L2=478.87um
	L3=178.03um	L3=376.34um	L3=445.07um
	L4=199.44um	L4=419.15um	L4=392.11um
	L5=161.13um	L5=371.83um	L5=436.06um
	L6=157.75um	L6=429.30um	L6=422.54um

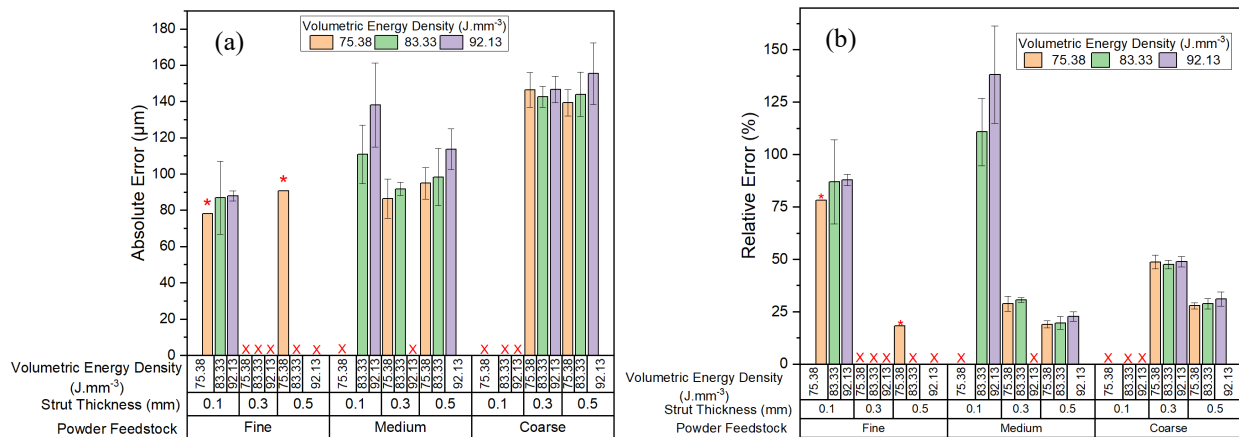


Figure 6: (a) Absolute Error and (b) Relative Error (%) of thin struts at different energy density. The red 'X' represents complete missing sample and red "*" represents results with only one sample.

3.4. Effects on areal porosity, and areal pore size

Internal defects in L-PBF of Ti6Al4V are attributed to unstable melt flow, keyholes due to evaporation of Al and V and internal pores from the feedstock powder, insufficient melting of local layer-layer contacts, and ~8% liquid-to-solid shrinkage for Ti6Al4V [39]. Porosity from processing is mainly due to lack-of-fusion or keyholing [40, 41]. Keyholes pores are formed at higher energy densities where the vapor bubbles are trapped within the melt pool, whereas lack of fusion pores are formed at lower energy density where some regions remain unmelted [40]. Due to the higher -than-nominal energy density setting parameters in this study, the majority of pores were expected to be of keyhole type with circularity close to 1, which was verified as shown in the Fig.7. Based on the single-track studies performed using Ti6Al4V powder, the keyhole pores diameter ranges from 8 μm - 127 μm (i.e., areal pore size range: 50 μm^2 – 50,671 μm^2) [40, 42, 43], and most of the pores identified in this study areal pore size are within this range (Fig.8b). Furthermore, the Fig.7d-f clearly shows the increase in number of defects with increase in input volumetric energy density. This increase in defects is expected to be cause for lower success rate of thin struts at higher energy density levels. The highest areal porosity and pore sizes was observed at the input energy density of 92.13 J.mm⁻³. The statistical analysis performed on the available data points showed that powder feedstock, strut dimension and volumetric energy density have significant ($p < 0.05$) effects on areal porosity, whereas only strut dimension and volumetric energy density have significant ($p < 0.05$) effect on pore size. Both average areal porosity and pore size were found to be consistent ($p > 0.05$) along the build direction. Fig.8a-b show the average areal porosity and average areal pore size of thin strut samples.

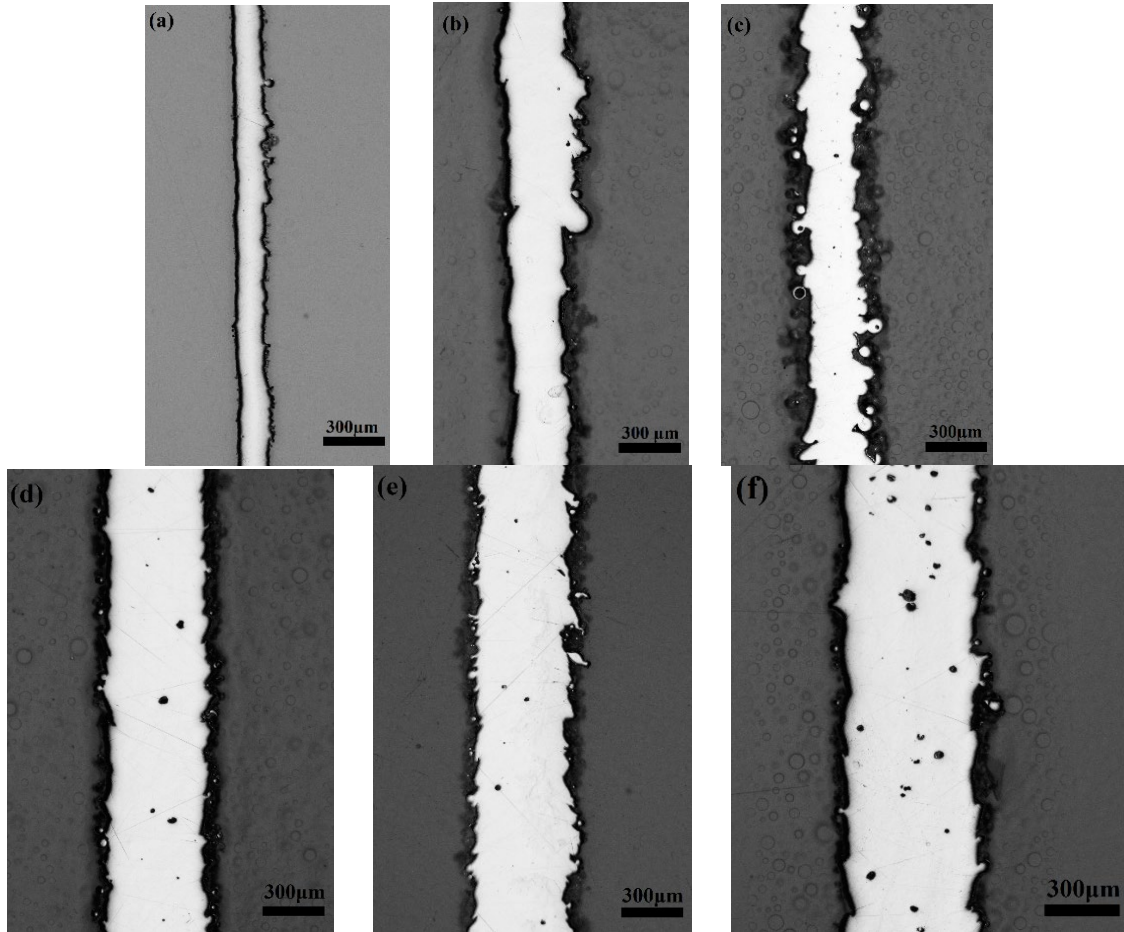


Figure 7: (a-c) Areal Porosity of thin strut samples at baseline process settings (a) 0.1mm fine powder feedstock, (b) 0.3 mm medium powder feedstock, and (c) 0.3 mm coarse powder feedstock. (d-f) 0.5 mm medium powder feedstock at different energy density (d) 75.38 J.mm⁻³ (e) 83.33 J.mm⁻³ (f) 92.13 J.mm⁻³

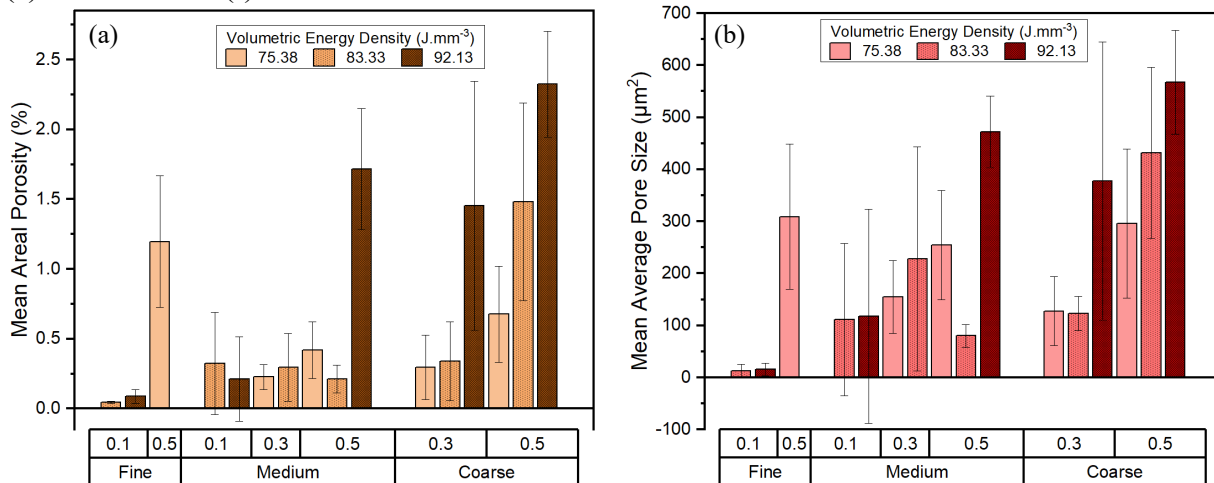
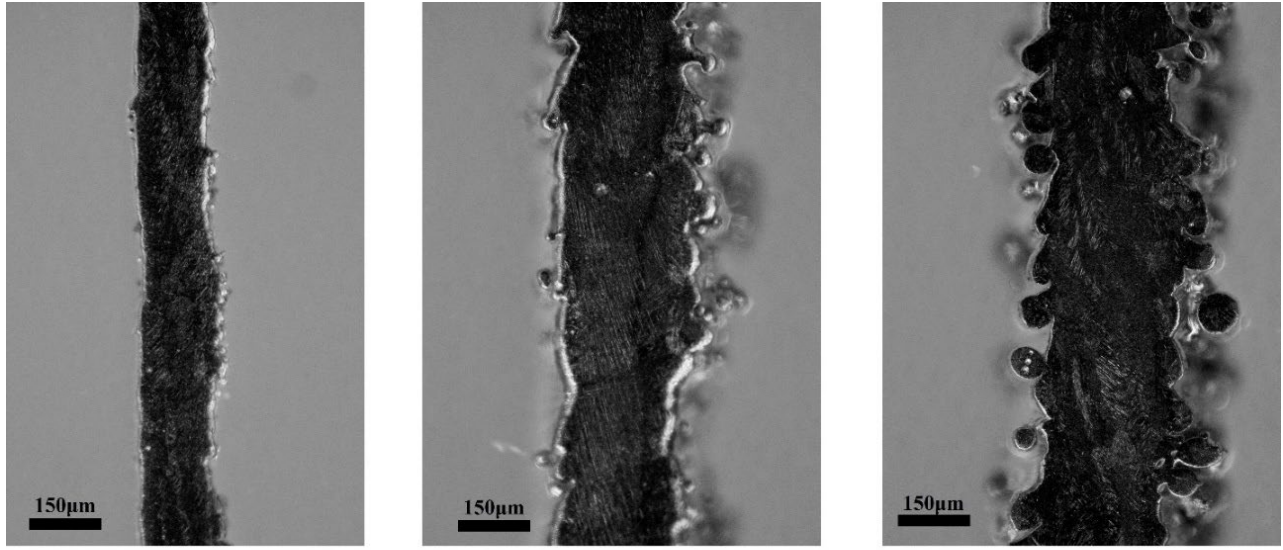


Figure 8: (a) Average areal porosity and (b) Average pore size of thin strut features at different energy density. Due to low success rate, no Tukey pairwise comparison was performed. Graphs does not include the missing samples.

Zhang et al. [35] and Delcuse et al. [44] reported decreasing trend of porosity with decrease of thin strut dimensions. For the feature dimension range in this study, similar decreasing porosity trend can be observed with decrease in strut diameters. Average pore size also showed decreasing trend with decrease in strut diameters. Overall, the pores size appears to exhibit broad ranges for individual samples whereas the effect of the thin feature dimension is relatively insignificant. Further checking with the scan paths generated by the EOS PSW3.5 control software showed that only contour scan was active in the 0.1 mm thin strut samples, whereas both contour and hatch scan were active in the 0.3 mm and 0.5mm samples. As the 0.1 mm samples are not exposed with hatch scan, the total areal input energy density is expected to be lower than for the 0.3 mm and 0.5 mm samples. On the other hand, the hatch scan for 0.3 mm and 0.5 mm samples could potentially leads to excessive heat input due to the frequent laser acceleration/deceleration and turning [41]. The input energy in this study is in higher than nominal value and excessive heat input at the turnaround locations could further exacerbate quality issues such as dimension, porosity, and pore size for the 0.3mm and 0.5 mm strut samples.

3.5.Effects on microstructure and grain width

The grain microstructure of thin features fabricated using different powder feedstock are shown in the Fig. 9a. Columnar grains growing along the build direction were observed. Similar to the study by Zhang et al. [45], the grain width in the strut center along the diameter direction were identified to be larger than those located near the strut boundaries (Fig.9b). Small grains at the feature surface nucleate from adjacent powder particles at the part surface in the power bed and grow towards the center following the maximum temperature gradient [12]. Since the grain growth at surface is inhibited by the higher cooling rate at surface, the grain width at the strut boundaries were smaller than in the interior regions. The graph in the Fig. 9c indicates the variation of grain width of thin struts. For current study, the results clearly indicate the higher influence of thin strut dimension as compared to powder feedstock type and input energy density. The cooling effect of loose powders at strut boundaries are similar irrespective of the strut dimension. However, with increase in strut diameter, the strut boundary cooling effect reduces, promoting the formation of more number of grains in the center. However, the grain width of the center grains is larger than boundary grains. Thus, higher number of larger center grains in larger diameter thin strut results in overall grain width increment. More regular grain morphology towards the center interior of the feature is also partially attributed to the continuous growth of columnar grain due to heterogeneous grain growth. Similar to porosity, for 0.3mm samples the increase in particle size distribution resulted in decrease in grain width. On the other hand, the grain width of 0.5mm were largely consistent across different powder feedstocks. This might imply that as the feature dimension increases, the solidification and cooling process within the L-PBF-AM gradually achieves stabilized status with the bulk of the features, and therefore the dependency of grain width on the powder feedstock size gradually diminishes.

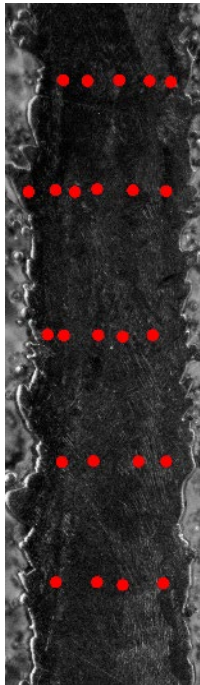


Fine Powder 0.1 mm Thin Strut

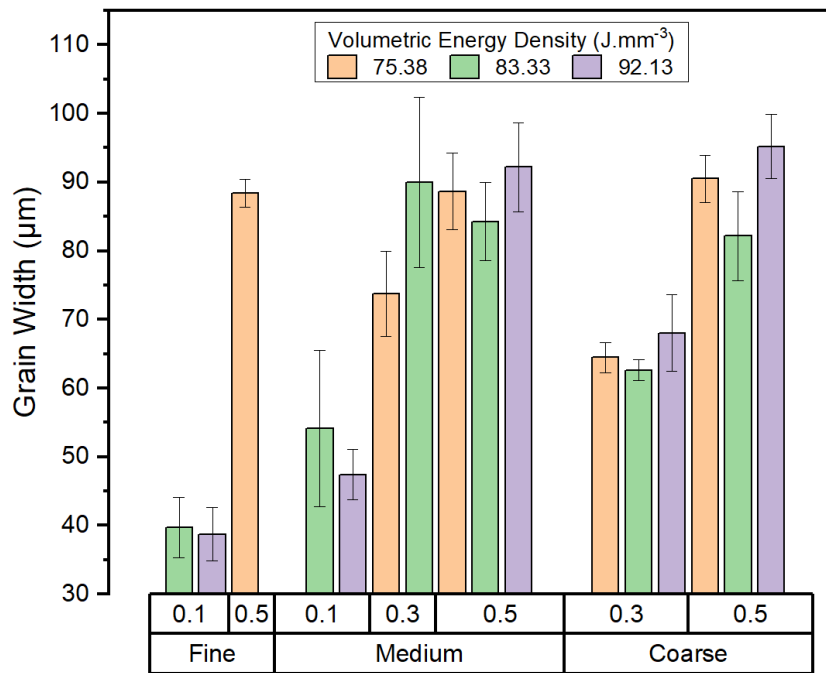
Medium Powder 0.3 mm Thin Strut

Coarse Powder 0.3 mm Thin Strut

(a)



(b)



(c)

Figure 9: (a) Thin Strut Grain microstructure of different powder feedstock (b) 0.5mm medium powder feedstock thin strut sample showing interior grain boundaries indicated with red dots (c) Average grain width of thin strut samples at different energy density

3.6.Effects on feature mechanical strength

Three-point bending test were employed to evaluate the flexural modulus, flexural yield strength and ultimate flexural strength of different samples, and the results are presented in Fig.10. Sun et al. [46] studied the effects of build direction on mechanical performance of L-PBF additively manufactured Ti6Al4V at input energy density level of 58.33 J.mm⁻³, and reported

the ultimate flexural strength to be between 948 MPa (at 0° build orientation) to 1026 MPa (at 90° build orientation). In this present study, 0.5 mm thin strut fabricated with coarse powder feedstock showed lowest value of average mechanical properties (i.e., flexural modulus of 13.54 GPa, flexural yield strength of 737.34 MPa, and ultimate flexural strength of 1392.07 MPa) at input energy density level of 75.38 J.mm⁻³. The yield point was identified using the derivative approach developed by Christensen [47]. The stress-strain curve within the approximate elastic-plastic region was first fitted with 5-order or 6-order polynomial function, and the yield point was then identified as the first local maxima point of the 2nd derivative of the stress-strain function. The overall yield strength calculation approach is briefly illustrated in the Fig.11. Based on the calculated individual sample yield strength, the flexural modulus was then calculated from the identified elastic regions.

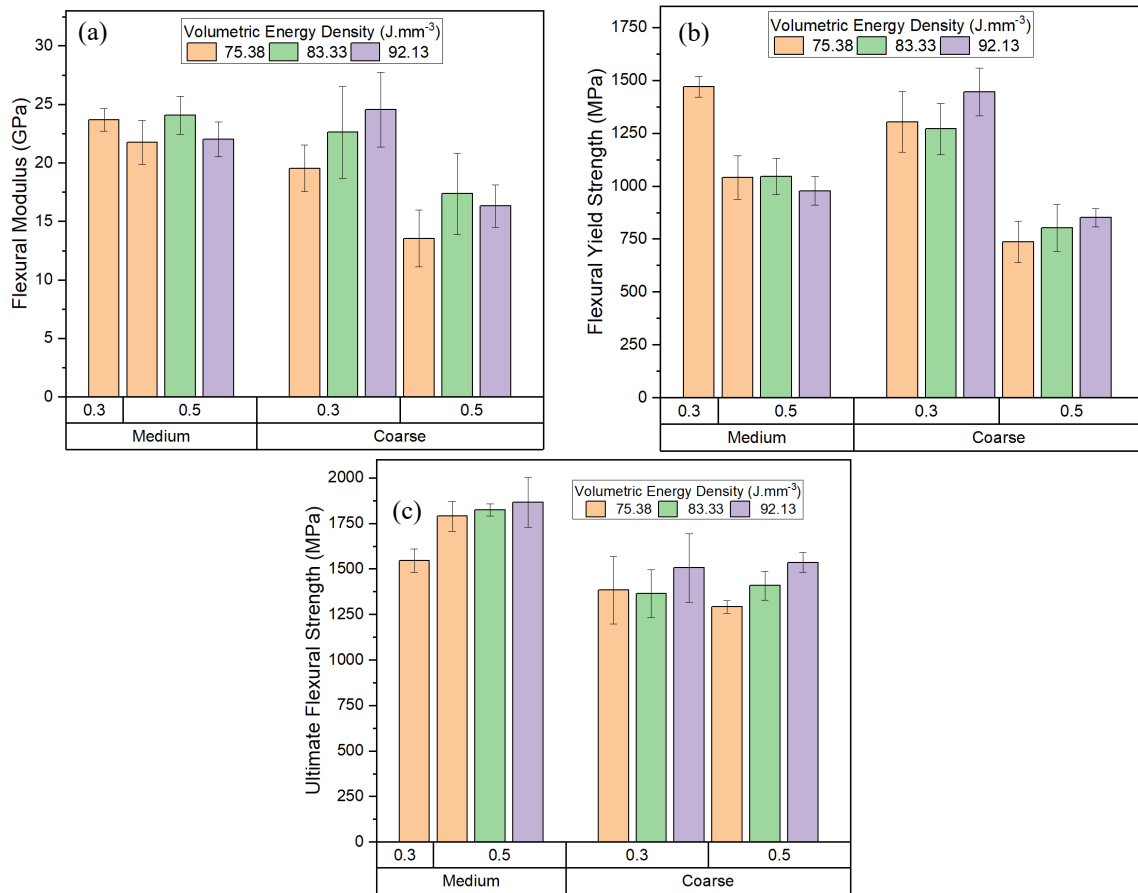


Figure 10: Mechanical properties of thin strut samples at different energy density (a) Flexural modulus (b) Flexural Yield Strength and (c) Ultimate Flexural Strength

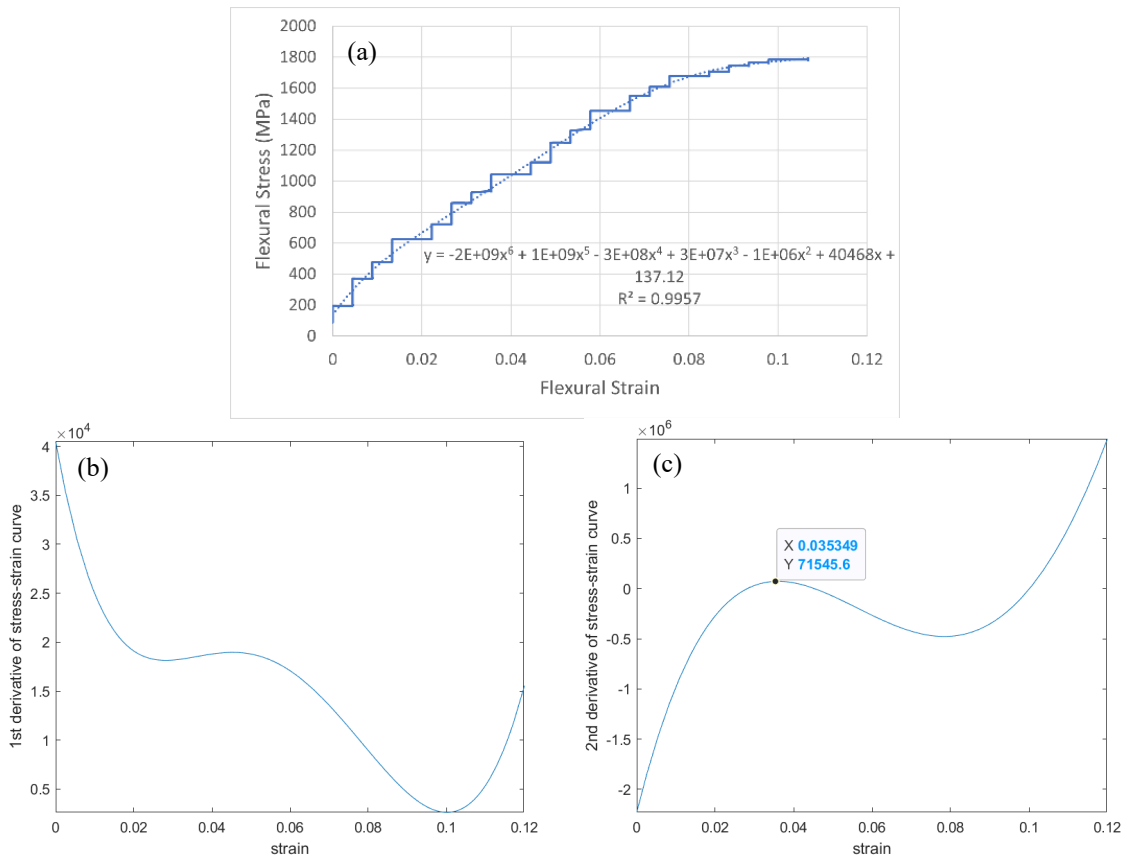


Figure 11: Yield Strength analysis from stress-strain curve based on derivative approach (a) Stress-strain curve (b) First derivative of stress-strain curve Vs strain (c) Second derivative of stress-strain curve Vs strain

From the results, the effect of the strut diameter was more significant on flexural modulus and flexural yield strength, and less significant on ultimate flexural strength. Comparing between the medium and coarse powder feedstock, the coarse powder feedstock appears to negatively affect the mechanical properties of the struts, which is particularly significant with larger-size struts (0.5mm). Such observation was in good agreement with the observed trends with porosity and pore size discussed earlier, which increase with increase in strut size and powder particle size distribution. On the other hand, despite the expectation of lower mechanical properties at highest energy density level (i.e., 92.13 J.mm^{-3}), in this study the effect of energy density for a given strut diameter were observed to be less significant compared to the powder feedstock type and strut dimension.

4. Conclusions

The thin strut features of dimensions varying from 0.1mm to 0.5mm were fabricated using L-PBF-AM process and the effect of different Ti6Al4V powder size (fine, medium, and coarse) at three different volumetric energy density i.e., 75.38 J.mm⁻³, 83.33 J.mm⁻³ and 92.13 J.mm⁻³ were studied. A systematic sequential methodology was developed and implemented for careful characterization and testing of the thin struts. Since the present study utilized higher-than-nominal input energy density, utilization of lower input energy density close to nominal values are recommended for higher fabrication success rate. Within the range of process parameters studied in this work, bimodal powder size distribution is expected to yield better fabrication success rate. More importantly, both thin strut dimension and powder feedstock size distribution were highly influential factor from strut quality aspect. Based on the results on fabrication success rate, dimensional accuracy, porosity, and pore size, microstructure grain size and different mechanical properties, coupling effect with compound PPG-M relationships were observed for thin strut features. Therefore, this study elucidates the necessity of further in-depth studies on small dimensional scales for L-PBF-AM process such that the knowledge base on the thin features L-PBF-AM process can be re-established.

Declaration of Competing Interest

The authors declare no conflict of interest.

Acknowledgements

This project was partially supported by the Praxair Surface Technologies TruForm Ambition Grant. The authors would like to acknowledge the support of Additive Manufacturing Institute of Science & Technology (AMIST) Center at University of Louisville, for experimental resources and consulting for this project.

References

1. Nazir, A., et al., *A state-of-the-art review on types, design, optimization, and additive manufacturing of cellular structures*. The International Journal of Advanced Manufacturing Technology, 2019. **104**(9): p. 3489-3510.
2. Wu, Y. and L. Yang, *The effect of unit cell size and topology on tensile failure behavior of 2D lattice structures*. International Journal of Mechanical Sciences, 2020. **170**: p. 105342.
3. Nečemer, B., M. Vesenjāk, and S. Glodež, *Fatigue of Cellular Structures-a Review*. Strojniski Vestnik/Journal of Mechanical Engineering, 2019. **65**(9).
4. Wu, Y. and L. Yang, *Elastic and failure characteristics of additive manufactured thin wall lattice structures with defects*. Thin-Walled Structures, 2021. **161**: p. 107493.
5. Wu, Y. and L. Yang, *Modeling of the effect of local material imperfection to the structural mechanical property variability of 2D finite-size cellular structures*. Composite Structures, 2021. **262**: p. 113610.
6. Reinhart, G., S. Teufelhart, and F. Riss, *Investigation of the geometry-dependent anisotropic material behavior of filigree struts in ALM-produced lattice structures*. Physics Procedia, 2012. **39**: p. 471-479.
7. Ahuja, B., et al., *Developing LBM process parameters for Ti-6Al-4V thin wall structures and determining the corresponding mechanical characteristics*. Physics Procedia, 2014. **56**: p. 90-98.
8. Yang, L., et al. *An investigation of thin feature generation in direct metal laser sintering systems*. in *2014 International Solid Freeform Fabrication Symposium*. 2014. University of Texas at Austin.
9. Miranda, G., et al., *A study on the production of thin-walled Ti6Al4V parts by selective laser melting*. Journal of Manufacturing Processes, 2019. **39**: p. 346-355.
10. Hossain, U., et al., *Mechanical and morphological properties of additively manufactured SS316L and Ti6Al4V micro-struts as a function of build angle*. Additive Manufacturing, 2021. **46**: p. 102050.
11. Weißmann, V., et al., *Comparison of Single Ti6Al4V Struts Made Using Selective Laser Melting and Electron Beam Melting Subject to Part Orientation*. Metals, 2017. **7**(3): p. 91.

12. Leicht, A., U. Klement, and E. Hryha, *Effect of build geometry on the microstructural development of 316L parts produced by additive manufacturing*. Materials Characterization, 2018. **143**: p. 137-143.
13. Murchio, S., et al., *Additively manufactured Ti-6Al-4V thin struts via laser powder bed fusion: Effect of building orientation on geometrical accuracy and mechanical properties*. Journal of the Mechanical Behavior of Biomedical Materials, 2021. **119**: p. 104495.
14. Vrána, R., et al., *Selective laser melting strategy for fabrication of thin struts usable in lattice structures*. Materials, 2018. **11**(9): p. 1763.
15. Wang, X., et al., *Microstructure and mechanical properties of stainless steel 316L vertical struts manufactured by laser powder bed fusion process*. Materials Science and Engineering: A, 2018. **736**: p. 27-40.
16. Vock, S., et al., *Powders for powder bed fusion: a review*. Progress in Additive Manufacturing, 2019. **4**(4): p. 383-397.
17. Spierings, A.B. and G.N. Levy. *Comparison of density of stainless steel 316 L parts produced with selective laser melting using different powder grades*. 2009.
18. Alfaiy, A., J.T. Hughes, and K. Ridgway, *Critical evaluation of the pulsed selective laser melting process when fabricating Ti64 parts using a range of particle size distributions*. Additive manufacturing, 2018. **19**: p. 197-204.
19. Brika, S.E., et al., *Influence of particle morphology and size distribution on the powder flowability and laser powder bed fusion manufacturability of Ti-6Al-4V alloy*. Additive Manufacturing, 2020. **31**: p. 100929.
20. Riener, K., et al., *Influence of particle size distribution and morphology on the properties of the powder feedstock as well as of AlSi10Mg parts produced by laser powder bed fusion (LPBF)*. Additive Manufacturing, 2020. **34**: p. 101286.
21. Sinico, M., A. Witvrouw, and W. Dewulf. *Influence of the Particle Size Distribution on Surface Quality of Maraging 300 Parts Produced by Laser Powder Bed Fusion*. in *Proceedings of the Special Interest Group Meeting on Advancing Precision in Additive Manufacturing*. 2019. Nantes, France.
22. Spierings, A.B., N. Herres, and G. Levy, *Influence of the particle size distribution on surface quality and mechanical properties in AM steel parts*. Rapid Prototyping Journal, 2011. **17**(3): p. 195-202.
23. Brika, S.E. and V. Brailovski, *Influence of Powder Particle Morphology on the Static and Fatigue Properties of Laser Powder Bed-Fused Ti-6Al-4V Components*. Journal of Manufacturing and Materials Processing, 2020. **4**(4): p. 107.
24. Jelis, E., et al., *L-PBF of 4340 Low Alloy Steel: Influence of Feedstock Powder, Layer Thickness, and Machine Maintenance*. Journal of Materials Engineering and Performance, 2019. **28**(2): p. 693-700.
25. Sun, Y.Y., et al., *Manipulation and Characterization of a Novel Titanium Powder Precursor for Additive Manufacturing Applications*. JOM, 2015. **67**(3): p. 564-572.
26. Balbaa, M.A., et al., *Role of powder particle size on laser powder bed fusion processability of AlSi10mg alloy*. Additive Manufacturing, 2021. **37**: p. 101630.
27. Groarke, R., et al., *316L Stainless Steel Powders for Additive Manufacturing: Relationships of Powder Rheology, Size, Size Distribution to Part Properties*. Materials, 2020. **13**(23): p. 5537.
28. Cao, L. and W. Guan, *Simulation and analysis of LPBF multi-layer single-track forming process under different particle size distributions*. The International Journal of Advanced Manufacturing Technology, 2021. **114**(7): p. 2141-2157.
29. Snow, Z., A.R. Nassar, and E.W. Reutzler, *Invited Review Article: Review of the formation and impact of flaws in powder bed fusion additive manufacturing*. Additive Manufacturing, 2020. **36**: p. 101457.
30. Gong, H., et al. *Defect Morphology in Ti-6Al-4V Parts Fabricated by Selective Laser Melting and Electron Beam Melting*. 2013.
31. *ASTM E112-13, Standard Test Methods for Determining Average Grain Size*. 2013: ASTM International, 100 Barr Harbor Drive, PO Box C700, West Conshohocken, PA 19428-2959. United States. p. 28.
32. Averardi, A., et al., *Effect of particle size distribution on the packing of powder beds: A critical discussion relevant to additive manufacturing*. Materials Today Communications, 2020. **24**: p. 100964.
33. Gong, H., et al., *Analysis of defect generation in Ti-6Al-4V parts made using powder bed fusion additive manufacturing processes*. Additive Manufacturing, 2014. **1-4**: p. 87-98.
34. Promoppatum, P., R. Onler, and S.-C. Yao, *Numerical and experimental investigations of micro and macro characteristics of direct metal laser sintered Ti-6Al-4V products*. Journal of Materials Processing Technology, 2017. **240**: p. 262-273.
35. Zhang, S., *Design, analysis, and application of a cellular material/structure model for metal based additive manufacturing process*. 2017.

36. Hollander, D.A., et al., *Structural, mechanical and in vitro characterization of individually structured Ti-6Al-4V produced by direct laser forming*. *Biomaterials*, 2006. **27**(7): p. 955-963.
37. Van Bael, S., et al., *Micro-CT-based improvement of geometrical and mechanical controllability of selective laser melted Ti6Al4V porous structures*. *Materials Science and Engineering: A*, 2011. **528**(24): p. 7423-7431.
38. Yang, L., et al., *Use of electropolishing for uniform surface treatment of metal components with complex external geometries*. 2021, Google Patents.
39. Zhang, X.Z., et al., *Toward Manufacturing Quality Ti-6Al-4V Lattice Struts by Selective Electron Beam Melting (SEBM) for Lattice Design*. *JOM*, 2018. **70**(9): p. 1870-1876.
40. Shrestha, S., T. Starr, and K. Chou, *A study of keyhole porosity in selective laser melting: single-track scanning with micro-CT analysis*. *Journal of Manufacturing Science and Engineering*, 2019. **141**(7).
41. Wu, Z., S.P. Narra, and A. Rollett, *Exploring the fabrication limits of thin-wall structures in a laser powder bed fusion process*. *The International Journal of Advanced Manufacturing Technology*, 2020. **110**(1): p. 191-207.
42. Bayat, M., et al., *Keyhole-induced porosities in Laser-based Powder Bed Fusion (L-PBF) of Ti6Al4V: High-fidelity modelling and experimental validation*. *Additive Manufacturing*, 2019. **30**: p. 100835.
43. Thanki, A., et al., *Study of keyhole-porosities in selective laser melting using X-ray computed tomography*. 2019.
44. Delcuse, L., et al., *Effect of powder bed fusion laser melting process parameters, build orientation and strut thickness on porosity, accuracy and tensile properties of an auxetic structure in IN718 alloy*. *Additive Manufacturing*, 2020. **36**: p. 101339.
45. Zhang, S., et al. *Property evaluation of metal cellular strut structures via powder bed fusion AM*. in *2015 International Solid Freeform Fabrication Symposium*. 2015. University of Texas at Austin.
46. Sun, W., et al., *Effects of the Build Direction on Mechanical Performance of Laser Powder Bed Fusion Additively Manufactured Ti6Al4V under Different Loadings*. *Advanced Engineering Materials*, 2021. **23**(12): p. 2100611.
47. Christensen, R.M., *Observations on the definition of yield stress*. *Acta Mechanica*, 2008. **196**(3): p. 239-244.